minerals

MDPI

Article

Process Mineralogy of Lithium and Rubidium in the Diantan Polymetallic Mining Area, Tengchong, Southwest China

Liming Ouyang [1,2], Jianqi Zhou [1], Huan Li [1,*], Majid Ghaderi [3], Wenbo Sun [1], Yiming Xie [1] and Xiaofan Li [1]

[1] Key Laboratory of Metallogenic Prediction of Nonferrous Metals and Geological Environment Monitoring, Ministry of Education, School of Geosciences and Info-Physics, Central South University, Changsha 410083, China; 225002060@csu.edu.cn (L.O.); 215011013@csu.edu.cn (J.Z.); sunwbo@csu.edu.cn (W.S.); 225011074@csu.edu.cn (Y.X.); lixiaofan@csu.edu.cn (X.L.)
[2] Land Space Survey and Monitoring Institute in Hunan Province, Changsha 410129, China
[3] Department of Economic Geology, Tarbiat Modares University, Tehran 14115-175, Iran; mghaderi@modares.ac.ir
* Correspondence: lihuan@csu.edu.cn

Abstract: Highly differentiated granite often contains abundant key metal resources, such as lithium and rubidium. The Tengchong area of Yunnan hosts a large number of highly differentiated granites from the Cretaceous age. Among these, granite samples from the Diantan tin–lead–zinc polymetallic mining area exhibit Li contents exceeding 0.02% and Rb contents surpassing 0.1%. This suggests a promising potential for Li and Rb mineralization. However, the occurrence status and process mineralogical characteristics of Li and Rb remain unclear, directly impacting the assessment of the region's comprehensive utilization potential for these key metals. This study focuses on representative granite samples from the Diantan mining area to conduct petrographic and process mineralogical research, examining single mineral chemical composition, physical properties, element occurrence state, and mineral embedding particle size. The results indicate that mica minerals primarily contain Li, while both feldspar and mica minerals are the main carriers of Rb. Zinnwaldite not only contains the highest Rb proportion among the samples but also plays a significant role in Li occurrence. Based on the dissociation characteristics, it is recommended to grind the material to a fineness of −0.075 mm, comprising 80% of the particles, before proceeding to the final flotation process. This would result in approximately 95% dissociation of the mica in the sample. Since mica is predominantly distributed between quartz and feldspar particles, with relatively low binding force, it facilitates mineral dissociation during the grinding process. Therefore, the actual beneficiation process may consider a moderately coarser grinding fineness based on the aforementioned findings.

Keywords: process mineralogy; highly differentiated granite; rubidium; lithium; MLA

check for updates

Citation: Ouyang, L.; Zhou, J.; Li, H.; Ghaderi, M.; Sun, W.; Xie, Y.; Li, X. Process Mineralogy of Lithium and Rubidium in the Diantan Polymetallic Mining Area, Tengchong, Southwest China. *Minerals* **2024**, *14*, 369. https://doi.org/10.3390/min14040369

Academic Editors: Jaroslav Dostal, Maria Economou-Eliopoulos and Martiya Sadeghi

Received: 1 February 2024
Revised: 25 March 2024
Accepted: 28 March 2024
Published: 30 March 2024

1. Introduction

Lithium and rubidium are crucial metals that play significant roles in national economic development [1–4]. Lithium, the lightest known metal, is widely utilized in various fields such as lightweight Li alloys, Li batteries, hydrogen bombs, rockets, nuclear submarines, and new jet aircraft. Rubidium and its compounds find applications in biomedical research, electronics, fiber optic communication, special glass, and fireworks [1–4].

In nature, Rb and Cs are typically associated with deposits of alkali metals (Li, K) and rare metals (Be, Nb, Ta, etc.), with only a few independent deposits [1–4]. Lithium and Rb mineralization is commonly associated with highly differentiated granite, making the study of their occurrence and process mineralogy an important research focus [5–8]. As dispersed elements, Li, and Rb are typically found within primary rock-forming minerals of granite, such as mica and feldspar. The particle size, chemical composition, and physical properties of these host minerals directly affect the extraction of key metals like Li and

Rb [9–12]. Therefore, understanding the process mineralogical characteristics is crucial for the recycling and utilization of Li and Rb associated with granite.

The Diantan Sn-Pb-Zn polymetallic deposit in Tengchong, Yunnan, is located in the Tengchong Block of the Southwest Three Rivers Tethys tectonic domain. It represents the northern extension of the well-known southeast Asian tin polymetallic mineralization belt [13–17], primarily yielding Sn, Pb, Zn, and fluorite deposits. Recent mineral exploration has shown that the granite associated with the Sn-Pb-Zn deposits in the mining area is highly differentiated and evolved, suggesting significant mineralization potential for key metals such as Li and Rb. The granite samples from this area exhibit Li content exceeding 0.02% and Rb content surpassing 0.1%. However, the current understanding of the occurrence and process mineralogical characteristics of these key metals is uncertain, directly impacting the assessment of their comprehensive utilization potential in the mining areas.

In this study, representative granite samples were selected for analysis and testing from the Diantan mining area. The study focuses on granite petrology, mineralogy, and process mineralogy, including the chemical composition of individual minerals, physical phases, elemental occurrence states, and mineral particle sizes. These findings will provide a foundation for the comprehensive recovery and utilization of key metals such as Li and Rb in the mining area. Additionally, those will offer valuable insights into evaluating the economic potential of similar types of granite in the region.

2. Geological Background

The Tengchong Block comprises exposed multi-level granite and a Middle Neoproterozoic basement, along with scattered sedimentary rocks from the Silurian, Devonian, Upper Carboniferous, Lower Permian, and Cretaceous periods, as well as minor outcrops of Quaternary volcanic rocks (Figure 1a,b) [17,18]. Within the Tengchong Block, three primary faults can be identified: the Gaoligongshan Fault, the Qipanshi Tengchong Fault, and the Dayingjiang Fault, all exhibiting NE–SW orientation. Granite related to polymetallic mineralization constitutes over 50% of the area within the Tengchong Block, forming the Sn-W Tengchong Lianghe granite belt [19,20].

The Diantan Sn-Pb-Zn polymetallic mining area in Yunnan is situated in the northern part of the Tengchong Block. There are two main mining parts in the area, Dadongshan and Xiangchunyuan (Figure 1c). The exposed strata in the mining area mainly belong to the Upper Carboniferous period (Figure 1b). These strata are mainly distributed in the Dadongshan area, consisting of gray to grayish black brecciated speckled feldspar quartz sandstone, which generally displays brecciation. Additionally, locally-formed feldspar-bearing quartz biotite hornfels and biotite hornfels are present. On the western side of the mining area, there are layers of gray thin to medium-thick carbonaceous and sandy clay-slate, with hornfelsized quartz sandstone at the top. Influenced by regional structures, the overall structure in the area trends in a nearly N–S direction, featuring well-developed fault structures (Figure 1c). There are primarily two groups of faults: an early NE or near-NE oriented group, including five faults (F1, F2, F3, F4, and F5), with F1 being the ore-bearing and controlling fault. In the later stage, an E–W or near E–W oriented group, represented by F10, a translational fault, is observed (Figure 1c). The Diantan granite in the Diantan area is located at the confluence of the Donghe granite belt and the Guyong granite belt within the Tengchong Block. The area has undergone multiple periods of Cretaceous magmatic activity, which is widespread and frequent. The ancient Yong granite group and the Donghe granite group in the area exhibit characteristics of multiple stages of magmatic activity (Figure 1a,b) [21]. Thermal contact metamorphism is primarily manifested by the metamorphism of clastic rocks at the contact zone of granite bodies and the edge of fractured structural zones, leading to the transformation of slate into spotted slate. Contact metasomatism is evident through the formation of angular rock zones in granite and the edge of the Carboniferous Kongshuhe Formation feldspar quartz sandstone in the structural fracture zone. Metasomatism results in the formation of uneven skarn blocks in the structural zone and biotitization in the granite. Regional tectonic movements have caused some areas to undergo regional light metamorphism, forming shallow metamorphic rocks such as slate and quartz sandstone. Fault tectonic activity induced dynamic metamorphism in certain rocks, leading to the formation of linearly distributed structural breccia and mylonites.

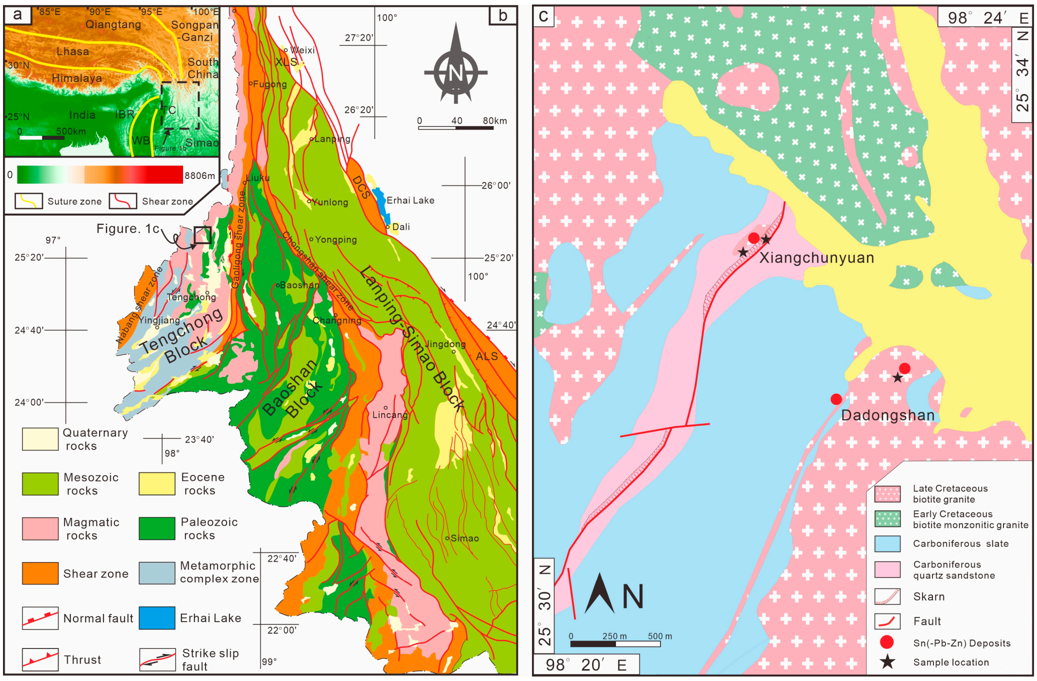

Figure 1. (**a**) Simplified tectonic map of the Tethyan system in southeast Asia, and location of the southeast Asia metallogenic belt in the Sibumasu Block (modified after [17]); (**b**) Geological map and major deposits of the Tengchong Block (modified after [20]); (**c**) Geological map and cross-section of the Diantan Sn deposit.

3. Sampling and Analytical Methods

3.1. Samples

The samples used in this study were collected from representative granite specimens obtained from the Dadongshan and Xiangchunyuan mining areas for subsequent analysis and testing. The sampling locations are indicated in Figure 1c. The samples from both mining areas include medium to fine-grained biotite granite characterized by block-like and granular structures. Within the rock mass, there are W-Sn polymetallic quartz veins and pegmatite veins, indicative of a highly differentiated granite body (Figure 2). Thin sections and polished slices were prepared for petrographic observation and testing. To ensure sample representativeness and reduce sampling errors, mica was crushed and graded. The samples were sieved into ten particle sizes to determine their particle size distribution and degree of dissociation: 0.83 mm, −0.83 + 0.59 mm, −0.59 + 0.42 mm, −0.42 + 0.30 mm, −0.30 + 0.21 mm, −0.21 + 0.15 mm, −0.15 + 0.105 mm, −0.105 + 0.074 mm, −0.074 + 0.052 mm, and −0.052 mm. The samples were crushed to simulate actual processing conditions, with a coarse crushing processing time of 3–4 min per kilogram. The fine crushing processing time used was 7–12 min per kilogram.

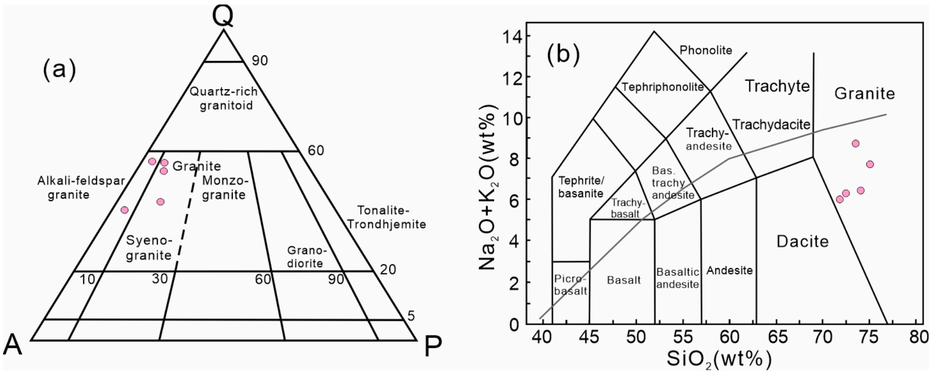

Figure 2. (**a**) QAP diagram for classification of rock types (modified after [22]); (**b**) SiO_2 vs. $Na_2O + K_2O$ (modified after [23]).

3.2. Whole-Rock Analyses

Sample preparation and major and trace element analyses were carried out at the ALS laboratory in Guangzhou, China. The samples were crushed in a steel jaw crusher and subsequently ground into a powder with particle sizes less than 200 mesh (74 µm) using an agate mortar. Each prepared sample (0.66 g) was fused with a 12:22 lithium tetraborate–lithium metaborate flux which also included an oxidizing agent (lithium nitrate), and it was then poured into a platinum mold. Major element contents were determined by X-ray fluorescence (XRF) spectrometry (Bruker D8 Advance diffractometer, Bruker Corporation, Billerica, MA, USA). Inductively coupled plasma mass spectrometry (ICP-MS) was employed to analyze rare earth and other trace elements. SARM-45 (South African Bureau of Standards, the Pretoria Republic of South Africa) and CCRMP (Canadian Certified Reference Materials Project) SY-4 were used as standards, and the analytical uncertainties were generally within 5%.

3.3. Mineralogical Analyses

The analysis of mineral parameters is conducted using the Mineral Liberation Analyzer (MLA) (FEI MLA 250, FEI Company, Hillsboro, OR, USA), which primarily consists of an FEI scanning electron microscope and an EDAX energy spectrometer (SEM-EDS). These hardware components are complemented by the ore automatic determination system software (QEMSCAN measurement software, version 5.3.2, FEI Company, Hillsboro, OR, USA). The automatic control system collects standard data and incorporates a database with over 500 minerals. The scanning electron microscope operates at an acceleration voltage range of 200 V–30 kV, with an amplification factor of 6×–1,000,000×. SEM-EDS analysis covers elements from Be^4 to U^{92} and supports both line and surface scanning.

By integrating electron microscopy software, SEM-EDS analysis technology, and MLA software (version 5.3.2), automatic sample displacement is achieved. The Back-Scattered Electron (BSE) image granulation processing enables the differentiation of various phases, along with the automatic collection of SEM-EDS data for accurate mineral identification using X-rays generated by the SEM-EDS. A sample mineral standard library is established, and process mineralogical parameters are obtained through computerized automatic fitting calculations.

For this test, a powdered sample (with particle size less than 1 mm after crushing) was utilized. The sample was fixed using resin bonding and subjected to an MLA scanning test to determine its content based on the proportion of mineral area. The use of powder sample reduction offers greater representativeness compared to direct scanning of thin films. The chemical phase analysis method for Li_2O, Rb_2O, etc., involves the following steps: (1) leaching Li_2O and Rb_2O in the sample using hydrochloric acid as a leaching agent, followed by determining their contents via inductively coupled plasma emission spectroscopy; (2) leaching the filter residue from the previous step using a leaching agent of 10% HCl–5% HF and determining its content through inductively coupled plasma emission spectroscopy; (3) calcinating the filter residue from the previous step, adding mixed acid, and determining the Li and Rb content in the volumetric flask liquid using inductively coupled plasma emission spectroscopy.

4. Results and Discussion

4.1. Chemical Composition of the Sample

Table 1 shows the results of chemical multi-element analysis on the granite samples. In addition, Tables 2 and 3 present the results of chemical phase analysis specifically targeting the main minerals mica and feldspar.

Table 1. Chemical multi-element analytical results of the granite samples.

Compositions	XCY-21	XCY-23	DDS-5	DDS-54	DDS-66
SiO_2 (wt.%)	73.76	72.19	72.86	75.15	73.97
TiO_2	0.03	0.09	0.07	0.03	0.09
Al_2O_3	15.68	17.57	16.73	14.34	15.26
TFeO	1.43	1.56	3.25	0.72	1.57
MnO	0.17	0.28	0.16	0.23	0.13
MgO	0.22	0.77	0.90	0.12	0.22
CaO	0.06	0.21	0.48	0.26	0.72
Na_2O	0.21	0.17	0.36	1.28	0.46
K_2O	8.59	5.74	5.25	6.55	5.73
Total	100.17	98.68	100.09	98.72	98.20
Nb (ppm)	81.4	78.6	105.5	74.4	92.4
Li	227.4	277.5	281.0	274.5	236.7
Rb	1070	1035	1160	1165	915
Sr	2.5	3.7	<0.1	15.6	1.8
Be	23.89	32.9	15.45	23.64	12.43
Ta	12.7	18.6	13.7	62.3	14.1

Table 2. Analytical results of mica composition by SEM-EDS (wt.%).

	No.	SiO_2	TiO_2	Al_2O_3	FeO	MnO	MgO	Na_2O	K_2O	Rb_2O	F	Total *
Zinnwaldite	1	38.18	1.85	20.28	22.91	1.11	1.35	0.71	8.43	0.56	3.12	98.50
	2	36.46	1.97	19.01	25.09	1.28	1.29	0.64	8.56	0.86	3.34	98.50
	3	40.62	1.42	23.81	17.56	0.95	1.29	0.58	8.49	0.58	3.20	98.50
	4	36.93	1.92	19.45	24.57	1.17	1.46	0.6	8.75	0.54	3.11	98.50
	5	36.98	1.84	20.31	23.72	1.26	1.31	0.72	8.39	0.54	3.12	98.50
	6	37.5	1.26	20.68	23.23	1.21	1.15	0.62	8.89	0.65	3.31	98.50
	7	37.3	2.27	18.78	24.73	1.22	1.28	0.67	8.37	0.73	3.12	98.50
	8	37.03	2.00	19.75	24.21	1.12	1.44	0.75	8.50	0.62	3.08	98.50
	9	38.33	1.17	21.08	22.39	1.13	1.06	0.54	8.81	0.87	3.12	98.50
	10	37.17	2.24	19.31	24.34	1.23	1.46	0.71	8.23	0.67	3.14	98.50
	11	37.8	1.88	21.92	22.5	1.04	1.3	0.80	7.44	0.67	3.15	98.50
	12	38.31	0.33	21.33	23.24	1.21	1.16	0.59	8.57	0.54	3.12	98.50
	13	37.29	2.34	19.35	23.91	1.15	1.3	0.58	8.57	0.77	3.24	98.50
	14	37.66	2.31	20.21	22.6	1.21	1.38	0.59	8.68	0.52	3.12	98.50
	15	38.56	0.74	21.96	21.86	1.13	1.25	0.74	8.43	0.64	3.19	98.50
	16	37.74	1.70	20.48	23.13	1.16	1.30	0.66	8.47	0.65	3.21	98.50
Muscovite	17	46.43	0.01	37.72	1.01	0.4	0.65	1.02	7.81	0.14	0.31	95.50
	18	45.21	0.07	28.36	9.05	0.43	0.99	0.68	9.01	0.65	1.05	95.50
	19	41.86	0.58	39.54	8.29	0.36	0.92	0.57	3.13	0.18	0.07	95.50
	20	48.65	0.11	38.52	2.19	0.04	0.65	0.36	4.63	0.11	0.24	95.50
	21	45.75	0.05	30.17	7.25	0.38	0.81	0.48	9.29	0.34	0.98	95.50
	22	46.98	0.06	30.14	6.24	0.35	0.69	0.47	8.98	0.44	1.15	95.50
	23	43.96	0.29	29.11	9.26	0.4	0.99	0.73	9.17	0.50	1.09	95.50
	24	43.62	0.25	29.12	9.37	0.42	0.87	0.65	9.26	0.49	1.45	95.50
	25	46.68	0.04	30.48	6.12	0.39	0.7	0.58	9.12	0.45	0.94	95.50
	26	44.77	0.04	29.12	8.50	0.53	0.78	0.54	9.79	0.45	0.98	95.50
	27	45.37	0.15	32.23	6.73	0.37	0.81	0.61	8.02	0.38	0.83	95.50
Average		40.79	1.08	25.18	16.57	0.84	1.1	0.64	8.29	0.55	2.21	

* According to the conversion results of zinnwaldite containing 1.5% H_2O and muscovite containing 4.50% H_2O.

Table 3. Analytical results of feldspar composition by SEM-EDS (wt.%).

	No.	SiO_2	Al_2O_3	FeO	MgO	CaO	Na_2O	K_2O	Rb_2O	Total
K-feldspar	1	63.28	21.38	0.08	0.45	0.01	2.58	12.19	0.03	100.00
	2	63.86	21.55	0.05	0.59	0.02	0.61	13.17	0.15	100.00
	3	63.49	21.34	0.03	0.56	0.03	1.82	12.52	0.21	100.00
	4	63.69	21.42	0.02	0.53	0.06	0.64	13.47	0.17	100.00
	5	63.3	21.59	0.1	0.6	0.04	2.05	12.18	0.14	100.00
	6	63.98	21.53	0.13	0.54	0.01	1.98	11.77	0.06	100.00
	7	63.3	21.35	0.08	0.54	0.03	1.41	13.14	0.15	100.00
	8	63.42	21.5	0.15	0.51	0.02	0.97	13.34	0.09	100.00
	9	65.6	21	0.05	0.46	0.04	0.91	11.84	0.1	100.00
	10	64.36	21.44	0.07	0.52	0.03	1.65	11.71	0.22	100.00
	11	64.22	21.43	0.02	0.48	0.01	0.77	12.92	0.15	100.00
	12	64.02	21.64	0.04	0.52	0.02	0.75	12.97	0.04	100.00
	13	63.5	21.63	0.09	0.45	0.06	0.73	13.44	0.1	100.00
	14	63.4	21.53	0.01	0.52	0.02	0.99	13.38	0.15	100.00
	15	63.58	21.55	0.18	0.37	0.01	0.61	13.44	0.26	100.00
	16	64.34	21.77	0.15	0.54	0.03	1.08	11.91	0.18	100.00
	17	62.55	21.72	0.05	0.66	0.04	0.88	13.94	0.16	100.00
	18	62.99	21.78	0.08	0.63	0.02	0.8	13.57	0.13	100.00
	19	63.3	21.8	0.03	0.54	0.01	0.83	13.33	0.16	100.00
	20	63.41	21.61	0.07	0.51	0.05	0.65	13.52	0.18	100.00
	21	63.67	21.53	0.07	0.53	0.03	1.14	12.89	0.14	100.00
Albite	22	64.79	22.86	0.04	0.47	1.06	10.48	0.28	0.02	100.00
	23	66.06	22.9	0.2	0.44	0.27	9.74	0.32	0.07	100.00
	24	65.96	22.25	0.02	0.49	0.09	10.98	0.2	0.01	100.00
	25	66.11	22.15	0.1	0.38	0.14	10.76	0.32	0.04	100.00
	26	66.5	22.28	0.03	0.44	0.09	10.48	0.16	0.02	100.00
	27	64.68	22.95	0.11	0.43	0.84	10.67	0.29	0.03	100.00
	28	66.1	22.23	0.09	0.32	0.23	10.65	0.36	0.02	100.00
	29	64.04	23.38	0.1	0.47	0.84	10.29	0.87	0.01	100.00
	30	65.85	22.14	0.12	0.51	0.16	10.97	0.17	0.08	100.00
	31	63.7	23.64	0.13	0.51	1.69	9.86	0.44	0.03	100.00
	32	64.3	25.3	0.08	0.41	0.96	8.61	0.32	0.02	100.00
	33	66.29	22.17	0.08	0.39	0.05	10.84	0.17	0.01	100.00
	34	65.84	22.47	0.06	0.44	0.18	10.7	0.23	0.08	100.00
	35	65.29	22.42	0.16	0.4	0.56	10.98	0.15	0.04	100.00
	36	65.69	22.45	0.02	0.48	0.17	10.85	0.32	0.02	100.00
	37	65.41	22.77	0.09	0.44	0.49	10.46	0.31	0.03	100.00
Average		64.28	21.96	0.08	0.5	0.19	4.4	8.49	0.094	

Tables 1–3 present the elemental composition of the five samples of K-feldspar. The average SiO_2 content is 73.38%, Al_2O_3 content is 15.91%, and Na_2O + K_2O content is 6.86%. Additionally, the average Li content is 179 ppm, Rb content is 1069 ppm, Nb + Ta content is 110 ppm, Be content is 21 ppm, and TFeO and MnO contents are 1.70 and 0.19%, respectively. The Li and Rb contents in the sample are about 10 times the abundance of Li and 8 times the abundance of Rb in the granites from China on average (Li $\approx$ 18 ppm, Rb $\approx$ 130 ppm; data from [24]). Based on these findings, Li and Rb are potential targets for metallurgical recovery, whereas the relatively low levels of Nb, Ta, and Be suggest limited comprehensive utilization value. The presence of Li is predominantly in mica minerals, indicating mica as the primary carrier mineral of Li_2O and a key focus for beneficiation and recovery. Similarly, Rb_2O is primarily distributed in feldspar and other silicate minerals, with Rb_2O accounting for 58.24 and 58.43% in feldspar and 39.56 and 38.20% in mica minerals. Consequently, mica also contains significant Rb_2O. The physical and chemical similarities between feldspar and quartz enable their simultaneous removal as gangue components during the sorting process, simplifying mineral processing and sorting. Considering the comprehensive

chemical composition, the samples can be preliminarily categorized as low-grade Li- and Rb-mineralized granites.

4.2. Mineralogical Composition

After conducting comprehensive studies, including microscopic identification, scanning electron microscopy analysis, and MLA determination, it was concluded that the samples share similar mineral types and relatively comparable contents. The primary discrepancy is that the small sample contains a small amount of kaolinite, which is attributed to the strong weathering of the specimen. The MLA test results reveal that both samples contain higher contents of quartz (39.82%), K-feldspar (32.15%), and albite (20.01%) in the non-metallic minerals category. Following closely are zinnwaldite (3.86%) and muscovite (2.32%). Aeschynite, topaz (0.16%), kaolinite (1.12%), rutile (0.08%), zircon (0.02%), thorite (0.02%), bastnaesite (0.01%), and almandine (0.01%) are present as minor minerals. The content of metallic minerals is very low, with occasional occurrences of columbite (0.29%) and limonite (goethite) (0.01%). Figure 3 depicts the MLA color chart.

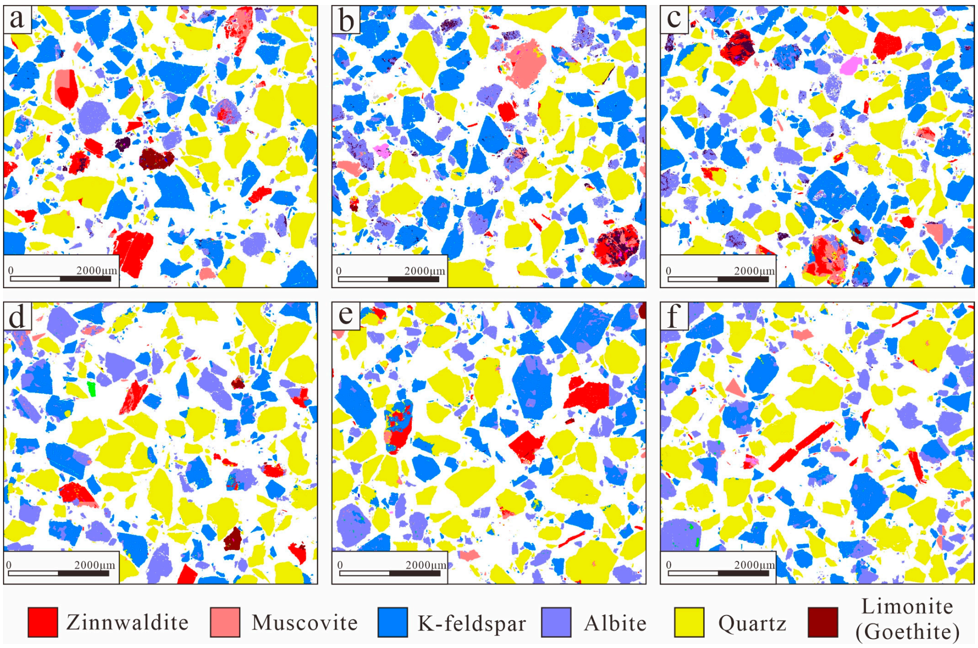

Figure 3. Diagram of MLA mineral composition of samples (**a**–**f**).

4.3. Mineral-Processing Properties of the Major Minerals

The processing product contains minerals such as mica and feldspar in all samples, exhibiting a high degree of consistency. In the subsequent section, we will comprehensively describe the main minerals observed in these samples by combining the microscopic characteristics and SEM scanning features of the samples' thin sections.

4.3.1. Mica

The dominant mineral in the sample is zinnwaldite (its content ranges from 4 to 5%), followed by muscovite (its content ranges from 2 to 3%). According to the SEM-EDS analytical results in Table 2, the structural formula of zinnwaldite is $KLi_xFe^{2+}{}_2Al_3Si_4O_{10}$ [F, $(OH)_n$], and the structural formula of muscovite is $K_2Al_8Si_9O_{10}$ [F_{3n}, $(OH)_n$].

Zinnwaldite displays well-developed sheet-like cleavage, appearing brownish-brown or brown-black when observed under plane-polarized light. It exhibits bright interference colors when viewed under crossed polars. The width of the mica flakes is generally uniform, ranging from 0.1 to 1 mm, with a few coarser grains reaching approximately 1.5 mm (Figures 4 and 5a–c,e,g–i). Scattered intergrowths between quartz or feldspar grains are common occurrences of zinnwaldite, sometimes forming aggregates and clusters.

The contact boundaries with feldspar and quartz are typically straight and regular. Some crystals undergo kaolinite alteration, while others persist as relics after being partly replaced by kaolinite. A small portion of zinnwaldite displays etched edges resembling gulfs due to quartz dissolution.

In contrast, muscovite is colorless and transparent under plane-polarized light, allowing easy differentiation from zinnwaldite. The width of muscovite flakes is relatively variable, generally ranging from 0.1 to 1 mm, with some finer grains measuring less than 0.05 mm. Muscovite primarily occurs as scattered intergrowths between quartz or feldspar grains, and in some instances, fine-grained muscovite transitions into the form of flaky sericite disseminated within the feldspar (Figure 5a–c,e,g–i). Based on these observations, it can be concluded that the crystal morphology of zinnwaldite and muscovite in the sample exhibits a relatively regular pattern. They predominantly fill the spaces between quartz and feldspar grains, demonstrating a relatively simple interlocking relationship. Consequently, it is anticipated that, after moderate grinding, a significant percentage of the mica will likely form individual or coarsely intergrown particles, which would facilitate further enrichment and recovery through flotation operations.

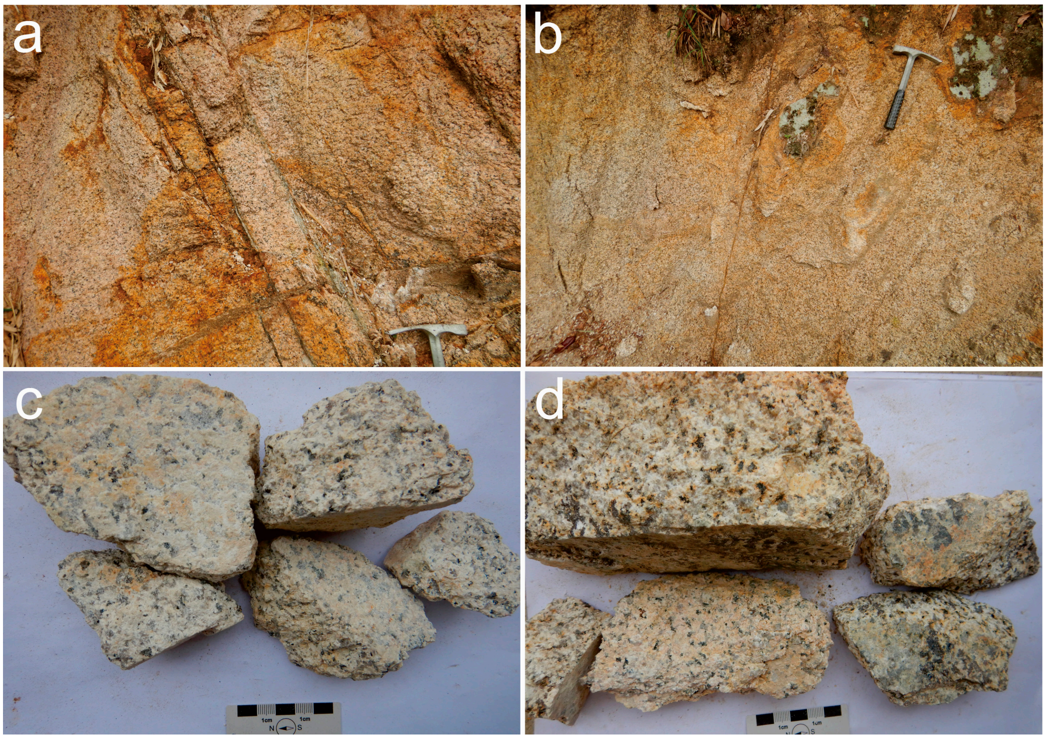

Figure 4. (**a**,**b**) Photos of granite field occurrence; (**c**,**d**) Photos of hand specimens of samples.

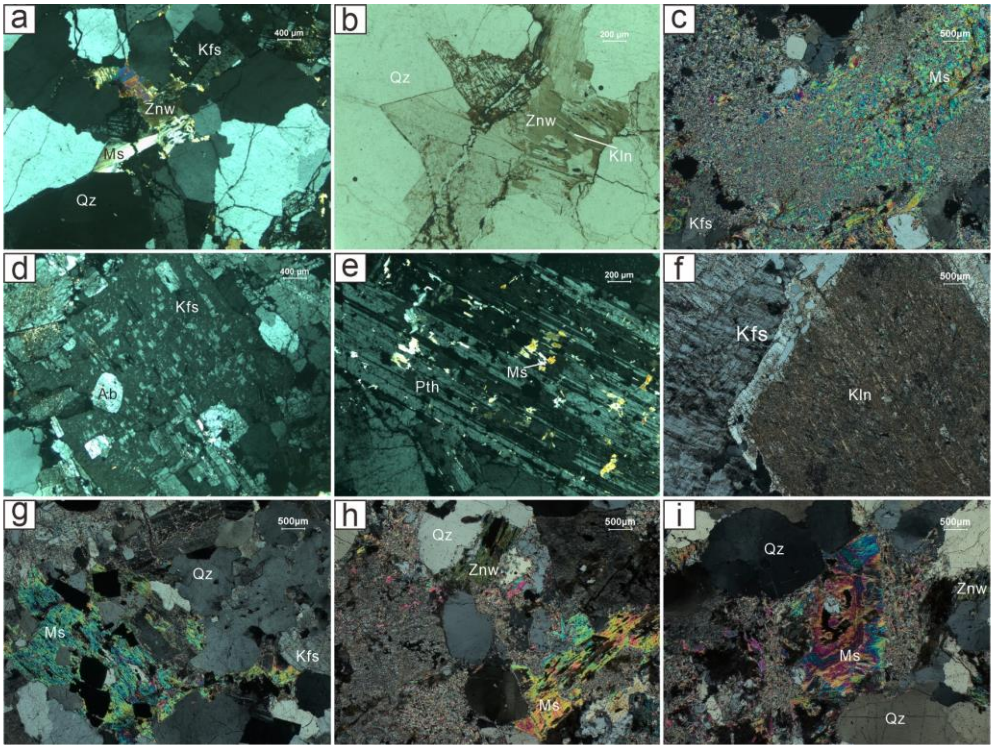

Figure 5. Photomicrographs of samples. (**a**) Zinnwaldite (Znw) is distributed in a substrate composed of quartz (Qz), K-feldspar (Kfs), and albite (Ab) (Crossed Polarized Light); (**b**) Zinnwaldite (Znw) is metasomatized by kaolinite (Kln) to form a sieve like structure (Plane Polarized Light); (**c**) K-feldspar (Kfs) has undergone high-temperature hydrothermal alteration, forming muscovite (Ms) (Crossed Polarized Light); (**d**) Albite (Ab) is distributed in K-feldspar (Kfs) (Crossed Polarized Light); (**e**) Muscovite (Ms) is distributed in small flakes in Perthite (Pth) (Crossed Polarized Light); (**f**) K-feldspar (Kfs) encapsulates kaolinite (Kln) (Crossed Polarized Light); (**g**) Muscovite (Ms) is partially metasomatized by quartz (Qz) in a harbor-like and sieve-shaped (Crossed Polarized Light) manner; (**h**) Muscovite (Ms) is scattered and disseminated along the intergranular filling distribution of K-feldspar (Kfs) and quartz (Qz) (Crossed Polarized Light); (**i**) Muscovite (Ms) surrounded by altered K-feldspar (Kfs) (Crossed Polarized Light). Mineral abbreviations are adapted from [25].

4.3.2. Feldspar

K-feldspar is the predominant mineral (with its content ranging from 30 to 35%), followed by albite (with its content ranging from 8 to 13%). According to the SEM-EDS analytical results in Table 2, the structural formula of K-feldspar is $K_3Al_5Si_{15}O_{39}$, and the structural formula of albite is $Na_{0.97}Ca_{0.03}Al_{1.12}Si_{3.14}O_8$.

K-feldspar is widely distributed and typically exhibits a regular subhedral tabular or columnar morphology. The K-feldspar grains are euhedral, with sizes ranging from 0.2 to 4 mm. It is closely intergrown with quartz and albite, and some grains contain minute inclusions of albite. Additionally, the surfaces of some grains may show slight kaolinization, while a small portion undergoes weak muscovitization. The presence of granular or irregular albite within K-feldspar suggests a high degree of magmatic evolution, classifying the host rock as a highly differentiated granitic rock (Figure 6).

Albite pertains to two textural types, with the primary one exhibiting a tabular or columnar shape and a grain size range similar to that of K-feldspar. Local occurrences of weak muscovitization may be observed. The secondary type appears as fine stripes, grains, or irregularly distributed crystals within K-feldspar (Figure 5a,c–g). Overall, whether it is K-feldspar or albite, most of the relationship with mica is relatively simple, with mica occurring as scattered interstitial fillings between their grains. The boundaries between them are relatively regular and smooth (Figure 6). It is anticipated that moderate grinding will result in sufficient dissociation of mica from feldspar.

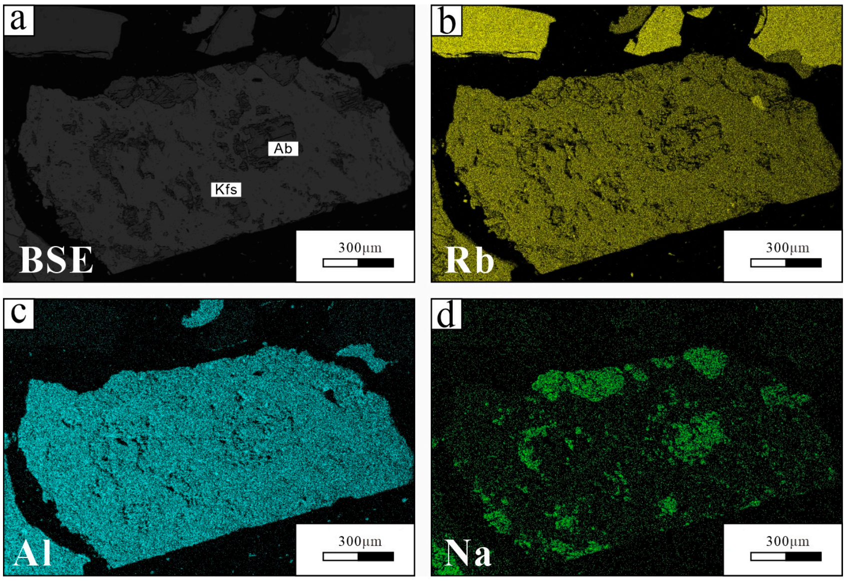

Figure 6. Granular and irregular albite (Ab) embedded in K-feldspar (Kfs). (**a**) SEM-BSE backscattered electron image; (**b**) SEM-Surface scanning image of Rb; (**c**) SEM-Surface scan image of Al; (**d**) SEM-Surface scan image of Na. Mineral abbreviations are adapted from [25].

4.3.3. Niobium-Tantalum Minerals

The main Nb- and Ta-bearing minerals are columbite and aeschynite. These minerals are randomly distributed, predominantly in small granular or columnar shapes that resemble needles. These often manifest as intermittent disseminated fillings found between quartz, feldspar, mica, or limonite (goethite) particles within cracks or along edges (Figures 7 and 8). Their particle size typically falls below 0.05 mm, and their content is less than 1%. Therefore, due to their extremely low content, fine particle size, and random dispersion within the sample, effectively enriching and recovering columbite and aeschynite through mineral processing is expected to present significant challenges.

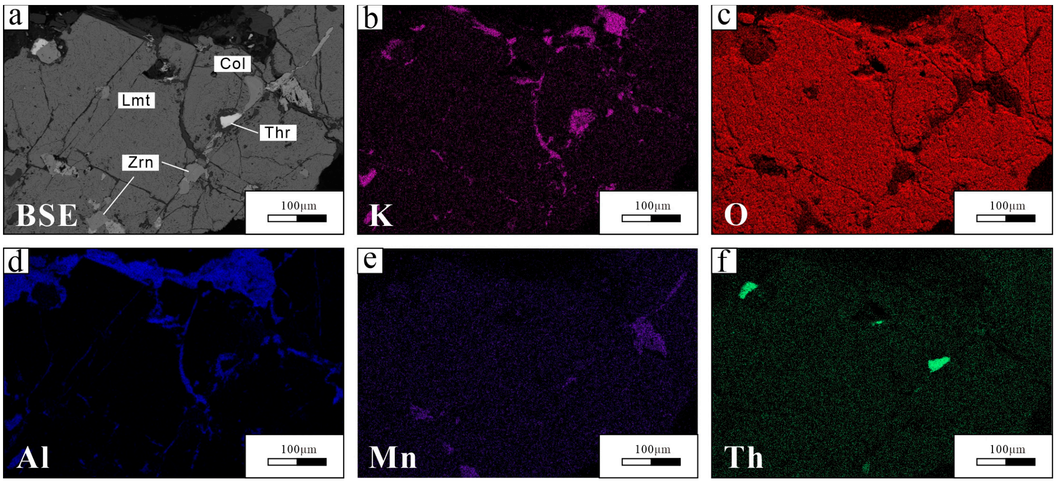

Figure 7. Fine granular columbite (Col), zircon (Zrn), and thorianite (Thr) are filled and distributed along the fractures, intergranular, or edge of limonite (Lmt). (**a**) BSE backscattered electron image; (**b**) Surface scanning image of K; (**c**) Surface scanning image of O; (**d**) Surface scanning image of Al; (**e**) Surface scanning image of Mn; (**f**) Surface scanning image of Th. Mineral abbreviations are adapted from [25].

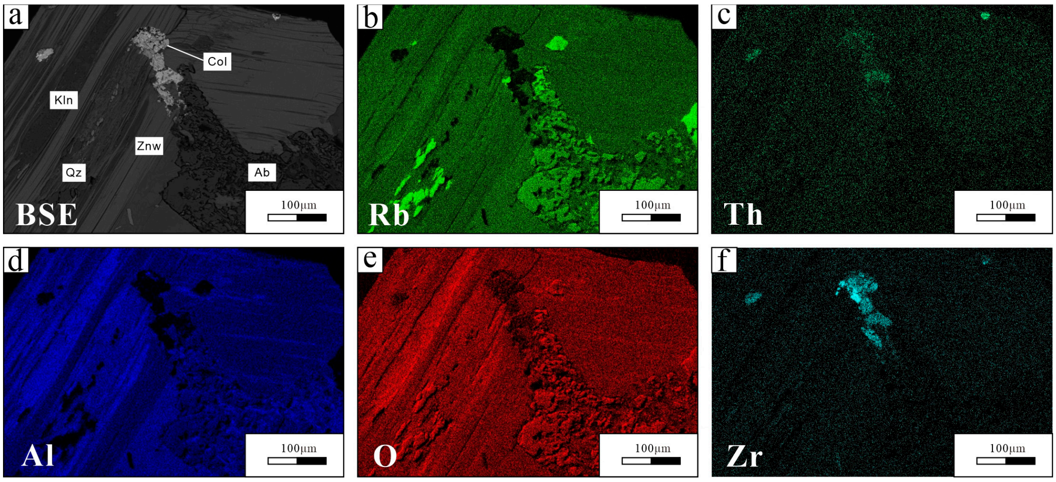

Figure 8. Columbite (Col) is embedded between the grains of zinnwaldite (Znw) and albite (Ab), filled with kaolinite (Kln) and quartz (Qz). (**a**) SEM-BSE backscattered electron image; (**b**) Surface scanning image of Rb; (**c**) Surface scanning image of Th; (**d**) Surface scanning image of Al; (**e**) Surface scanning image of O; (**f**) Surface scanning image of Zr. Mineral abbreviations are adapted from [25].

4.3.4. Rare Earth Minerals

The content of the rare earth minerals is exceedingly low (Table 1), comprising bastnaesite and monazite. The particle size is very fine, generally less than 0.03 mm. Particles are dispersed among or situated at the edges of quartz, feldspar, mica, and other minerals. Occasionally, it is enclosed within biotite and muscovite, with the particle size primarily below 0.03 mm (Figure 9). Owing to the extremely low content, fine particle size, and high dispersion of bastnaesite and monazite in the sample, effectively enriching and recovering them through mineral processing is also extremely challenging.

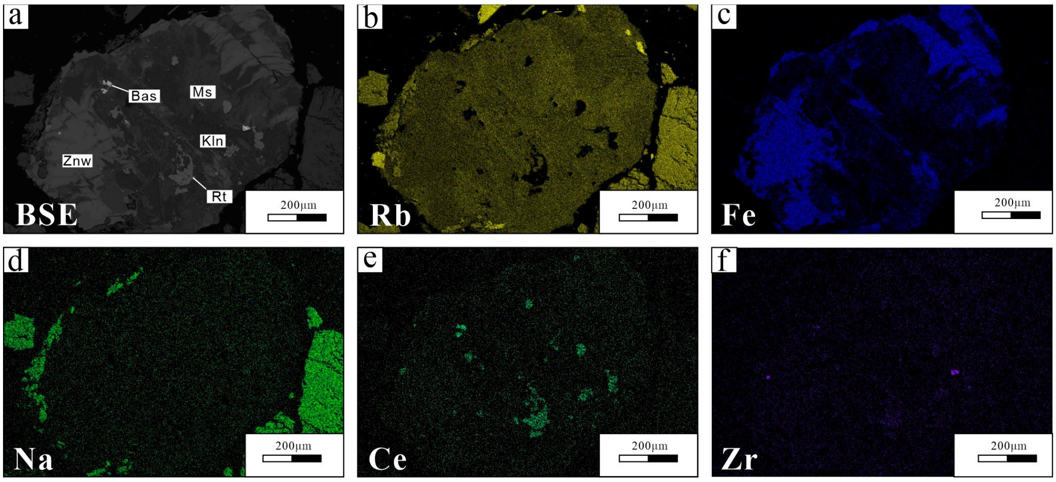

Figure 9. Bastnaesite (Bas) and rutile (Rt) are wrapped in the aggregate of zinnwaldite (Znw), muscovite (Ms), and kaolinite (Kln). (**a**) SEM-BSE backscattered electron image; (**b**) Surface scanning image of Rb; (**c**) SEM-Surface scanning image of Fe; (**d**) Surface scanning image of Na; (**e**) Surface scanning image of Ce; (**f**) Surface scanning image of Zr.

4.3.5. Quartz

Quartz is one of the primary constituent minerals in the sample, with its content ranging from 45 to 55%. Based on its proximity to mica and feldspar inlays, the quartz within the sample can be classified into two types. The first type exhibits irregular granular shapes with a particle size typically ranging between 0.2 and 5 mm. This type also shows a slight wavy extinction characteristic due to stress. Moreover, muscovite is observed dispersed along the grain boundaries. However, their relationship with other minerals such as zinnwaldite, muscovite, K-feldspar, and albite is not close. The second type of quartz is fine-grained and irregular in shape. It is closely mixed and embedded with feldspar, zinnwaldite, and muscovite. Their crystal size is generally uniform and relatively small, ranging from 0.02 to 0.15 mm (Figure 5a–c,e–h). These two types of quartz are mainly composed of the former type, with a mineral content ratio of approximately 95:5.

4.4. Chemical Composition of Mica and Feldspar

To determine the chemical composition characteristics of mica and feldspar, we utilized scanning electron microscopy to analyze the composition of various mica types (including zinnwaldite and muscovite) as well as different feldspar varieties (such as K-feldspar and albite) in our samples. The obtained results are presented in Tables 2 and 3 and Figure 10.

Based on our research, the following conclusions can be drawn: (1) As is well known, there is no independent mineral of rubidium in nature, but rather potassium is substituted in the lattice of mica or feldspar in the form of isomorphism [26–28]. Lithium mainly exists in Li-rich mica [29–31]. The average Rb_2O content in the mica samples from the two mining areas is relatively similar, with values of 0.55 and 0.53%, respectively (Figure 10). (2) Feldspar samples from the same areas have significantly lower Rb_2O contents compared to mica, measuring 0.10 and 0.12%, respectively. While feldspar has limited sorting value for Rb recovery rate, high concentrations of mixed feldspar in mica concentrate may impact Rb_2O grade. Our results demonstrate that mica not only has the highest Rb content in the sample but also serves as the primary mineral for Li. These values represent the theoretical Li_2O grade in mica concentrate during the enrichment process of ore dressing.

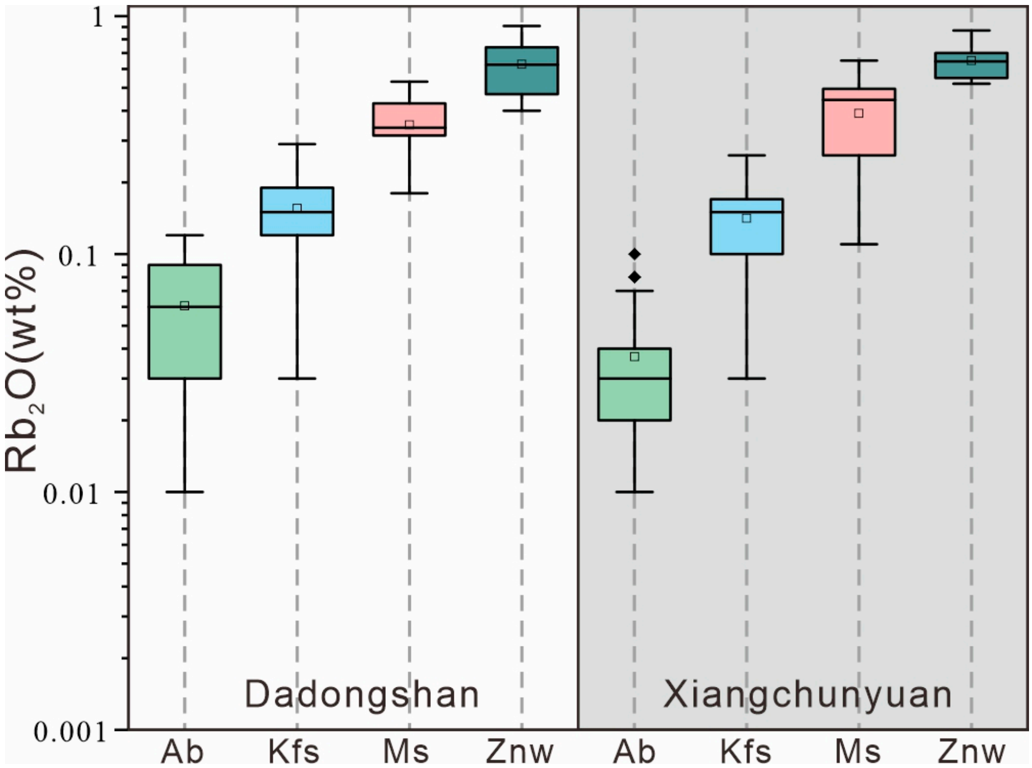

Figure 10. Box diagram of trace elements in mica and feldspar. Ab—albite; Kfs—K-feldspar; Ms—muscovite; Znw—zinnwaldite.

4.5. Particle Size Distribution of Mica

The particle size composition and distribution characteristics of the main target minerals in a sample have a direct impact on determining grinding fineness and formulating a reasonable beneficiation process. To this end, we conducted statistical analysis under a microscope to determine the embedding particle size of mica (including Fe-Li mica and muscovite) in samples from two mining areas. Figure 11 presents the results.

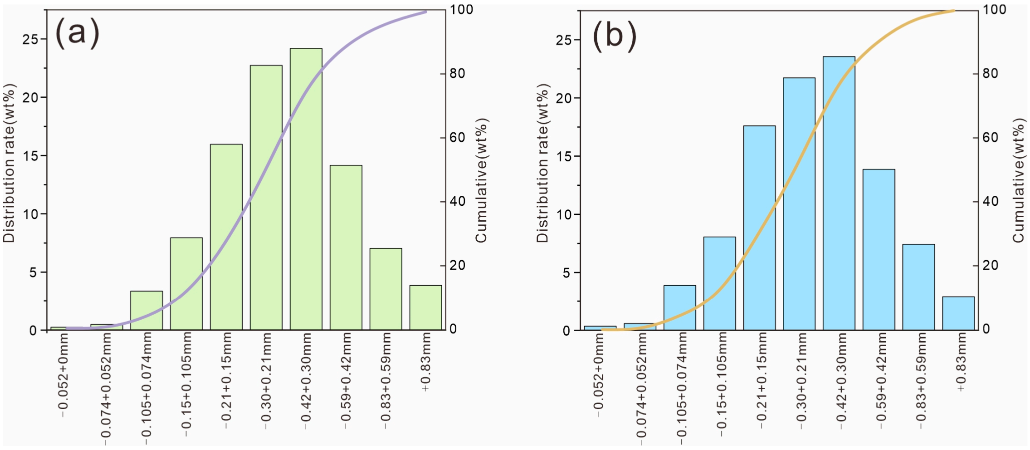

Figure 11. (**a**) Histogram and cumulative distribution curve of the particle size distribution of mica (including muscovite and zinc aluminate) in the Dadongshan sample; (**b**) Histogram and cumulative distribution curve of the particle size distribution of mica (including muscovite and zinc aluminate) in the Xiangchunyuan sample.

Our findings reveal that the mica in both samples has the characteristic of uneven distribution of fine particles. When the particle size is +0.105 mm, its positive cumulative distribution rates reach 95.90 and 95.18%, respectively. Based on the analysis of embedded particle size, to dissociate about 95% of the mica in the sample, it is appropriate to choose a grinding fineness of 0.105 mm when processing the samples in this zone. At this point, the −0.074 mm particle size accounts for approximately 80%. However, since most of the mica in the sample is filled and distributed between quartz and feldspar particles, the binding force between them is relatively low, which is conducive to the dissociation of minerals during the grinding process. Therefore, the actual beneficiation process can moderately coarsen the selected grinding fineness based on our findings. Previous studies on the recovery rate of mica from the same type (granite type) and the same particle size [31,32] demonstrate that the recovery rate of Li_2O in mica can exceed 90%.

5. Conclusions

(1) The granite in the mining area belongs to the low-grade Li-Rb granite type. The average Li_2O content in the samples is 0.056%, and the average Rb_2O content is 0.090%. Over 90% of the Li_2O in both samples exists in the mica minerals, while over 95% of the Rb_2O is present in the feldspar and mica minerals. Although the Li and Rb concentrations have not reached their current lowest industrial grades (Li: 0.3%; Rb: 0.1%), their volume is very large, indicating the potential for large-scale mining and significant value in comprehensive utilization and recovery.

(2) The samples represent typical granite with a relatively simple mineral composition. Quartz, Na-feldspar, and K-feldspar are the most abundant minerals, followed by Fe-Li mica, muscovite, and occasional traces of Nb-Fe mineral, pyroxene, and monazite. Iron-Li mica and muscovite are mainly found in the form of regular flakes scattered and disseminated between quartz or feldspar particles. Their association with feldspar and quartz is generally simple.

(3) The sample's feldspar comprises both K-feldspar and Na-feldspar, exhibiting subhedral plate-like columnar morphology, with particle sizes ranging from 0.2 to 5 mm. Overall, both types of feldspar have a relatively uncomplicated relationship with mica, displaying regular and flat boundaries. Consequently, moderate grinding is expected to achieve sufficient separation between mica and feldspar.

(4) The mica in the sample has a characteristic of uneven distribution of fine particles. Based solely on the analysis of embedded particle size, it is more appropriate to choose a grinding fineness of −0.075 mm, which accounts for 80% when processing samples in the area. At this point, about 95% of the mica in the sample can be dissociated. However, since mica is mostly filled and distributed between quartz and feldspar particles, the binding force between them is relatively low, facilitating the dissociation of minerals during the grinding process. Therefore, the selected grinding particle size in the actual beneficiation process can be moderately roughened based on the above estimation.

Author Contributions: Conceptualization, L.O., J.Z. and H.L.; methodology, W.S.; validation, Y.X. and L.O.; investigation, L.O., J.Z., H.L. and Y.X.; resources, L.O.; data curation, X.L., J.Z. and Y.X.; writing—original draft preparation, J.Z.; writing—review and editing, H.L., M.G. and X.L.; supervision, L.O.; project administration, Y.X.; funding acquisition, L.O. and H.L. All authors have read and agreed to the published version of the manuscript.

Funding: This study was supported by the National Natural Science Foundation of China (No. 92162103), the Natural Science Foundation of Hunan Province (No. 2022JJ30699, No. 2023JJ10064), and the Science and Technology Innovation Program of Hunan Province (No. 2021RC4055, No. 2022RC1182).

Data Availability Statement: Data supporting the findings of this study will be made available from the corresponding author upon reasonable request due to privacy.

Acknowledgments: We would like to express our gratitude to Engineer Jiang Jiangbo from Hunan Mining Research Institute for his support in the experiment, as well as to Yunnan Jingwei Mining Company for their support in our field exploration.

Conflicts of Interest: The authors declare no conflicts of interest.

References

1. Hu, X.J.; Li, H. Research progress and prospect of granitic pegmatite-type lithium deposits. *T. Nonferr. Metal. Soc.* **2021**, *31*, 3468–3488. (In Chinese with English Abstract)
2. Liu, H.L.; Nie, L.S.; Wang, X.Q.; Chi, Q.H.; Wang, L.J. Regional geochemical distribution and controlling factors of lithium in the Sino-Mongolia border areas. *Earth Sci. Metal. Soc.* **2022**, *47*, 2795–2808. (In Chinese with English Abstract)
3. Wise, M.A.; Curry, A.C.; Harmon, R.S. Reevaluation of the K/Rb-Li Systematics in Muscovite as a Potential Exploration Tool for Identifying Li Mineralization in Granitic Pegmatites. *Minerals* **2024**, *14*, 117. [CrossRef]
4. Biedilihan, T.; Abuduxun, N.; Huang, P.; Gan, J.; Talati, Y. Late Cryogenian Circum-Rodinia syn-subduction extension: Insights from highly fractionated S-type and A-type granitoids in the northern Tarim Craton. *Minerals* **2023**, *13*, 1446. [CrossRef]
5. Jiang, S.Y.; Su, H.M.; Zhu, X.Y. A new type of Li deposit: Hydrothermal crypto-explosive breccia pipe type. *J. Earth Sci.* **2022**, *33*, 1095–1113. [CrossRef]
6. Lai, X.; Chen, C.; Chen, X.; Fei, G.; Li, Y.; Wang, J.; Cai, Y. Process mineralogy characteristics of Lijiagou pegmatite spodumene deposit, Sichuan, China. *Minerals* **2023**, *13*, 1180. [CrossRef]
7. Chen, X.; Chen, C.; Lai, X.; Yang, Y.; Gu, Y.; Cai, Y. Whole-rock geochemistry and mica compositions in Lijiagou pegmatite spodumene deposit, western Sichuan, China. *Minerals* **2024**, *14*, 69. [CrossRef]
8. Lou, D.B.; Wang, D.H.; Li, W.Y. Progress of prospecting prediction research for granitic pegmatite-type lithium deposits at home and abroad. *Miner. Depos.* **2022**, *41*, 975–988. (In Chinese with English Abstract)
9. Fu, J.; Li, G.; Wang, G.; Guo, W.; Dong, S.; Li, Y.; Zhang, H.; Liang, W.; Jiao, Y. Geochemical evidence for genesis of Nb–Ta–Be rare metal mineralization in highly fractionated leucogranites at the Lalong Dome, Tethyan Himalaya, China. *Minerals* **2023**, *13*, 1456. [CrossRef]
10. Duan, Z.P.; Jiang, S.Y.; Su, H.M.; Zhu, X.Y.; Zou, T.; Cheng, X.Y. Trace and rare earth elements, and Sr isotopic compositions of fluorite from the Shihuiyao rare metal deposit, Inner Mongolia: Implication for its origin. *Minerals* **2020**, *10*, 882. [CrossRef]
11. Li, S.; Liu, J.; Han, Y.; Zhang, S. Review on the beneficiation of Li, Be, Ta, Nb-bearing polymetallic pegmatite ores in China. *Minerals* **2023**, *13*, 865. [CrossRef]
12. Timich, M.; Contessotto, R.; Ulsen, C. Process mineralogy of Li-enriched pegmatite combining laboratory mineral separations and SEM-based automated image analysis. *Minerals* **2023**, *13*, 343. [CrossRef]
13. Myint, A.Z.; Li, H.; Mitchell, A. Geology, mineralogy, ore paragenesis, and molybdenite Re-Os geochronology of Sn-W (-Mo) mineralization in Padatgyaung and Dawei, Myanmar: Implications for timing of mineralization and tectonic setting. *J. Asian Earth Sci.* **2018**, *95*, 575–592. [CrossRef]
14. Zhang, Z.W.; Shu, Q.; Yang, X.Y. Review on the tectonic terranes associated with metallogenic zones in Southeast Asia. *J. Earth Sci.* **2019**, *30*, 1–19. [CrossRef]

15. Roza Llera, A.; Fuertes-Fuente, M.; Cepedal, A.; Martin-Izard, A. Barren and Li–Sn–Ta mineralized pegmatites from NW Spain (Central Galicia): A comparative study of their mineralogy, geochemistry, and wallrock metasomatism. *Minerals* **2019**, *9*, 739. [CrossRef]
16. Zhao, R.Z.; Wang, M.F.; Li, H.; Shang, X.Y.; Ullah, Z.; Wang, J.P. Texture and geochemistry of scheelites in the Tongshankou deposit in Daye, Hubei, China: Implication for REE substitution mechanism and multistage W mineralization processes. *Minerals* **2021**, *11*, 984. [CrossRef]
17. Cao, H.W.; Zou, H.; Zhang, Y.H.; Zhang, S.T.; Zhang, L.K.; Tang, L.; Pei, Q.M. Late Cretaceous magmatism and related metallogeny in the Tengchong area: Evidence from geochronological, isotopic and geochemical data from the Xiaolonghe Sn deposit, western Yunnan, China. *Ore Geol. Rev.* **2016**, *78*, 196–212. [CrossRef]
18. Zou, H.; Cao, H.W.; Bagas, L.; Zhang, Y.H.; Zhang, S.T.; Zhang, Q.; Liu, H.; Li, Y. Origin of the Mo-bearing Xiaoshuijing Syenogranite in the Tengchong Terrane, SW China. *Ore Geol. Rev.* **2019**, *105*, 258–272. [CrossRef]
19. Xu, Y.G.; Yang, Q.J.; Lan, J.B.; Luo, Z.Y.; Huang, X.L.; Shi, Y.R.; Xie, L.W. Temporal–spatial distribution and tectonic implications of the batholiths in the Gaoligong–Tengliang–Yingjiang area, western Yunnan: Constraints from zircon U–Pb ages and Hf isotopes. *J. Asian Earth Sci.* **2012**, *53*, 151–175. [CrossRef]
20. Cui, X.L.; Wang, Q.F.; Deng, J.; Wu, H.Y.; Shu, Q.H. Genesis of the Xiaolonghe quartz vein type Sn deposit, SW China: Insights from cathodoluminescence textures and trace elements of quartz, fluid inclusions, and oxygen isotopes. *Ore Geol. Rev.* **2019**, *111*, 102929. [CrossRef]
21. Shen, Z.W.; Jin, C.H.; Zhang, H.; Zhang, Y.; Jiang, X.F. Zircon LA-ICP-MS U–Pb dating and geochemistry of monzonitic granite of Wujishan iron deposit in Yun-nan Province. *Mineral. Petrol.* **2013**, *33*, 53–59. (In Chinese with English Abstract)
22. Streckeisen, A.L. Classification and nomenclature of igneous rocks. *N. Jb. Miner.* **1967**, *107*, 144–240.
23. Middlemost, E.A.K. Naming materials in the magma/igneous rock system. *Earth Sci. Rev.* **1994**, *37*, 215–224. [CrossRef]
24. Shi, C.Y.; Yan, M.C.; Liu, C.M.; Chi, Q.H.; Hu, S.Q. Abundances of Chemical Elements in Granitoids of China and Their Characteristics. *Geochimica* **2005**, *34*, 470–482. (In Chinese with English Abstract)
25. Whitney, D.L.; Evans, B.W. Abbreviations for names of rock-forming minerals. *Am. Mineral.* **2010**, *95*, 185–187. [CrossRef]
26. Xu, C.L.; Zhong, C.B.; Lyu, R.L.; Ruan, Y.Y.; Zhang, Z.Y.; Chi, R.A. Process Mineralogy of Weishan Rare Earth Ore by MLA. *J. Rare Earths* **2019**, *37*, 334–338. [CrossRef]
27. Zhou, Q.; Qin, K.; Tang, D.; Wang, C. A combined EMPA and LA-ICP-MS study of muscovite from pegmatites in the Chinese Altai, NW China: Implications for tracing rare-element mineralization type and ore-forming process. *Minerals* **2022**, *12*, 377. [CrossRef]
28. Lv, Z.; Cheng, H.; Wei, M.; Zhao, D.; Wu, D.; Liu, C. Mineralogical characteristic and beneficiation evaluation of a Ta-Nb-Li-Rb deposit. *Minerals* **2022**, *12*, 457. [CrossRef]
29. Galliski, M.Á.; Márquez-Zavalía, M.F.; Roda-Robles, E.; von Quadt, A. The Li-bearing pegmatites from the Pampean pegmatite province, Argentina: Metallogenesis and resources. *Minerals* **2022**, *12*, 841. [CrossRef]
30. Barros, R.; Kaeter, D.; Menuge, J.F.; Fegan, T.; Harrop, J. Rare element enrichment in lithium pegmatite exomorphic halos and implications for exploration: Evidence from the Leinster albite-spodumene pegmatite belt, southeast Ireland. *Minerals* **2022**, *12*, 981. [CrossRef]
31. Che, D.; Zheng, M.; Zhao, Y.; Zhang, Z.; Ye, C.; Xing, E.; Zhang, X.; Li, M. High degree of differentiation and enrichment of Li, Rb and Cs in potassic-ultrapotassic volcanic rocks: An example from the Lhasa Block, Tibet. *Minerals* **2023**, *13*, 342. [CrossRef]
32. Tian, M.; Zhang, H.X.; Zhao, H.Q. Analysis of occurrence state and comprehensive utilization study of rare metals in a mica mine. *Multipurp. Util. Miner. Resour.* **2021**, *5*, 97–105.